Nanoscale

Accepted Manuscript

This article can be cited before page numbers have been issued, to do this please use: C. Stelling, S. Fossati, J. Dostalek and M. Retsch, *Nanoscale*, 2018, DOI: 10.1039/C8NR05499A.

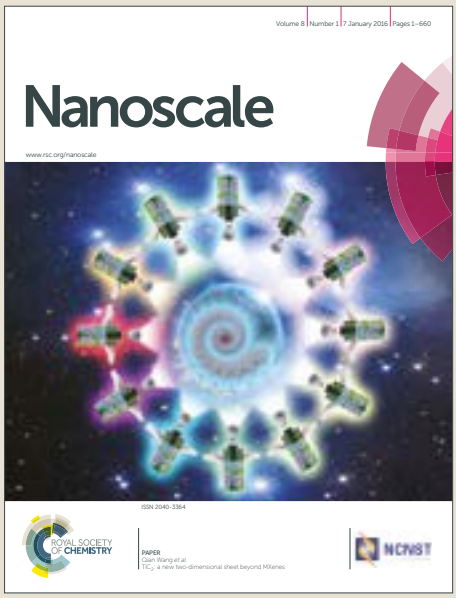

ROYAL SOCIETY OF CHEMISTRY

rsc.li/nanoscale

ROYAL SOCIETY OF CHEMISTRY View Article Online
DOI: 10.1039/C8NR05499A

Journal Name

ARTICLE

Surface Plasmon Modes of Nanomesh-on-Mirror Nanocavities Prepared by Nanosphere Lithography

Christian Stelling,[a] Stefan Fossati,[b] Jakub Dostalek,[b]* Markus Retsch[a]*

Received 00th January 20xx,
Accepted 00th January 20xx

DOI: 10.1039/x0xx00000x

www.rsc.org/

Metal-insulator-metal (MIM) structures show great potential for numerous photonic applications due to their ability to confine light energy to volumes with deeply sub-wavelength dimensions. Here, MIM structures comprising hexagonal gold nanohole arrays were prepared by nanosphere lithography. Angle-resolved UV-vis-NIR spectroscopy revealed a series of narrow, dispersive and non-dispersive modes, which were attributed to the excitation of surface plasmon polariton (SPP) modes. Applying finite-difference time-domain (FDTD) simulations and analytical diffraction phase-matching theory all resonances can be ascribed to only two SPP modes traveling at the outer gold surface and in the gap layer sandwiched between two metal films. Metamaterial resonances, as reported in the literature for similar structures, are not needed to explain the reflectance spectra fully. Bragg scattering of the symmetric gap SPP mode results in a gap resonance, which is insensitive to the angle of incidence over a broad angular range. The spectral position of this flat band can be controlled by tuning the grating period of the nanohole array as well as the thickness and the refractive index of the dielectric gap.

Introduction

Metallic nanohole arrays have been subject to extensive research after the seminal discovery of their extraordinary optical transmission.[1] They exhibit exceptional optical properties that are associated with the excitation of surface plasmon polariton (SPP) as well as localized surface plasmon (LSP) modes. As a consequence, metal nanohole arrays have been implemented into optical devices that serve as optical sensors[2], color filters[3] or transparent conducting electrodes.[4-6] When placed near an unperforated metal film, the arrays of nanoholes allows for the coupling of light to a metal-insulator-metal (MIM) structure. Such architecture exhibits rich characteristics including near perfect absorption[7-9] and coupling to magnetic resonances, similar to that found for nanoparticle arrays.[10, 11] Near perfect absorbers were realized at visible frequencies[7, 8] and for the near-infrared part of the spectrum.[9] The optical response of perforated MIM structure is often assigned to the excitation of Fabry-Pérot resonances in the trilayer structures[12, 13] as well as to the resonant excitation of coupled SPP modes located at the opposite metal/dielectric interfaces.[14]

Due to their relatively simple structure, perforated MIM-type metasurfaces can be readily prepared via lithographic methods.[8, 10] Thereby, the optical properties are mainly defined by the precisely tuned structure of the material. Top-down lithographic processes such as e-beam lithography or focused-ion-beam milling give structural control on the nanometer range, thus being capable of fabricating metamaterials for wavelengths down to the visible spectrum.[14] Nevertheless, for the sake of large-scale production, much effort is put into the development of solution-processed techniques, which capitalize on self-assembly methods.[15] Nanohole arrays coupled with thin metal films were, therefore, prepared using nanosphere lithography (NSL).[16] The wavelength of the primary resonance satisfied both the grating equation of the nanohole array and the Fabry-Pérot condition, thus showing a strong dependence on the distance between the nanohole array and the metal film.[13] Closely connected are nanohole-dielectric-nanohole structures, which equally show the existence of gap modes.[17-19]

Here we present a full and comprehensive understanding of a MIM structure, which is prepared by a facile and scalable implementation of NSL. The MIM architecture comprises a highly ordered nanohole array separated from a continuous gold film by a thin polymer layer. Using angle-resolved UV-vis-NIR spectroscopy, we were able to fully assign the rich plasmonic response of the resulting nanocavity arrays to diffraction coupling to only two SPP modes. We explored the structure-property relationship concerning the gap size and period of the nanohole arrays in detail and identified rules to prepare structures with remarkably narrow resonances exhibiting high absorption efficiency.

[a] Department of Chemistry, University of Bayreuth, 95447 Bayreuth, Germany
[b] Biosensor Technologies, AIT-Austrian Institute of Technology GmbH, Konrad-Lorenz-Strasse 24 | 3430 Tulln, Austria
Email: JD: Jakub.Dostalek@ait.ac.at; MR: Retsch@uni-bayreuth.de
Electronic Supplementary Information (ESI) available: Optical microscopy images, UV-vis-NIR spectra spectra of isolated metal nanohole array, UV-vis-NIR spectra of MIM structures with varying mirror thickness, angle-resolved UV-vis-NIR spectra of MIM structures with distinct insulator thickness and period, analytically derived dispersion curves of the SPP modes, AFM analysis of the plasma treated MIM structure, FDTD geometry. See DOI: 10.1039/x0xx00000x

View Article Online
DOI: 10.1039/C8NR05409A

Results and discussion

The preparation of the MIM structures starts with the fabrication of gold nanohole arrays on a sacrificial layer via NSL (Figure 1a). Subsequently, the nanohole arrays were transferred onto the target substrate comprising the readily prepared gap layer [poly(methyl methacrylate) (PMMA)] on top of a continuous gold film, following the recently published, interface-mediated method.[20] The process utilized in this paper allowed for fast and modular production of metasurface areas at square centimeter scale with highly uniform and reproducible optical properties.[21] However, techniques that allow the preparation of wafer-scale and larger sample areas are readily available.[22, 23] The homogeneity of the samples is restricted by point defects and grain boundaries within the monolayer but is highly uniform regarding the particle-particle spacing and the defect density. In Figure 1b the definition of the geometrical parameters of the assembled structures is illustrated. The lattice period p and the hole diameter d of the gold nanohole arrays are determined by the initial particle diameter and the particle diameter after plasma etching, respectively. The thickness of the bottom gold layer t_{gold}, the one of the PMMA gap gap layer t_{gap} and the thickness of gold film with nanohole arrays were controlled upon the deposition process. An SEM image of a typical sample is shown in Figure 1c.

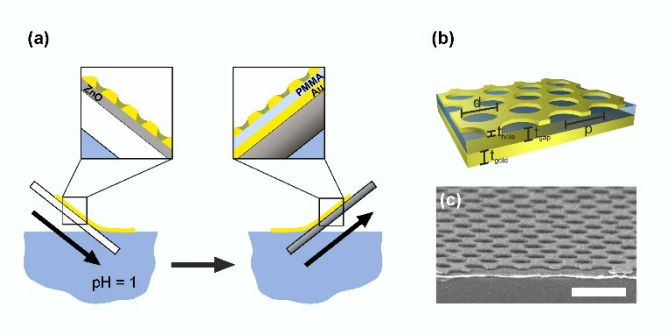

Figure 1. Metal-insulator-metal structures. (a) Scheme of transfer of gold nanohole arrays via the water/air interface. (b) Schematic illustration of the MIM geometry. (c) Side-view scanning electron microscopy image of a prepared MIM structure. Scale bar is 1 µm.

In order to characterize the optical properties of the prepared MIM nanostructures, a series of reflectance measurements were carried out for varied angles of incidence and wavelength in the visible and near-infrared part of the optical spectrum. Firstly, the reflectance measurements were performed at an angle of incidence fixed at $\Theta = 10$ ° for samples with different lattice period p. We chose periods of p = 375 nm, p = 570 nm, and p = 1040 nm while keeping the d/p ratio constant at 0.75. The thickness of the PMMA gap layer and the perforated metallic film was adjusted to $t_{gap} = 40$ nm and $t_{hole} = 90$ nm, respectively. As the thickness of the bottom gold layer was set to $t_{gold} = 100$ nm, the transmittance through the structure is negligible. As seen in the photographs in the inset of Figure 2 and the optical microscopy images (Figure S1), the samples with varied geometry exhibit distinct colors. The uniformity of these colors suggests an excellent spatial homogeneity over a sample area of > 1 cm² that can be fabricated on very short timescales. As can be seen in Figure 2, the perceived color of the gold MIM nanostructures is due to a series of narrow dips in the reflectivity spectrum, which occur in the visible and NIR part of the spectrum. In general, by increasing the lattice period p the spectral position of the reflectance dips shifts to longer wavelengths, see Figure 2. For example, the MIM nanostructure with p = 375 nm exhibits the most prominent reflectivity dip at a wavelength of 665 nm, while it is strongly redshifted to 926 nm for p = 570 nm and further to 1363 nm for p = 1040 nm. These resonances exhibit extraordinarily high Q-factors compared to other self-assembled materials.[24] The corresponding Q-factors (calculated by dividing the resonance wavelength by the full width at half minimum of the resonance) are equal to 14, 8 and 6 for the samples with periods of 375 nm, 570 nm, and 1040 nm, respectively. These high values are surprising considering the defects that are inevitable when using a bottom-up approach and support the robustness of our method. The dependence of the determined Q factors on the wavelength can be attributed to varied coupling strength for the chosen d/p ratio (which may cause over-coupling of the longer wavelength resonances) and higher sensitivity to defects of the lattice that is attributed to the increasing propagation length of SPPs with the wavelength.

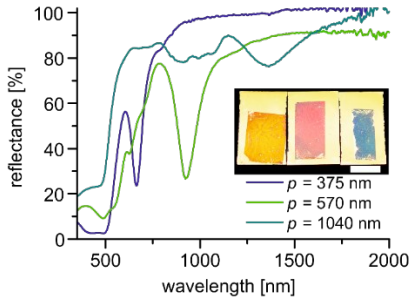

Figure 2. Influence of lattice period. Total reflectance of MIM structures with distinct lattice periods of the nanohole arrays measured at an angle of incidence of $\Theta = 10$ ° with unpolarized light. The inset shows a photograph of the macroscopic samples with p = 375 nm, p = 570 nm and p = 1040 nm (from left to right). Scale bar is 10 mm.

Additionally, a broad absorption band is visible below 500 nm which does not change with the period p and which originate from the decreased reflectivity from gold below its plasma frequency. The narrow dips occurring in the red and NIR part of the spectrum are attributed to the resonant excitation of SPP modes supported by the MIM structure with a dielectric gap layer sandwiched between the flat bottom gold layer and the gold film with the nanohole arrays. These resonances are not visible for nanohole arrays without the bottom gold layer (Figure S2) and rapidly vanishes when reducing the thickness of the bottom gold layer to a thickness comparable to the skin depth of gold (~ 20 -45 nm) (Figure S3). As soon as the bottom

gold film exceeds the skin depth of gold, however, the optical properties are hardly affected by the film thickness.[25]

To clarify the nature of the observed resonances, we performed reflectance measurements with incident angles between Θ = 6 ° and Θ = 60 °. Figure 3a shows an example of the measured spectra for a structure with p = 570 nm and t_{gap} = 50 nm. These results show a rich set of spectral features that shift with the angle of incidence, particularly at around 700 nm, and which appear non-dispersive for the resonance close to 900 nm. Additional reflectance dips are observed at longer wavelengths of around 1160 nm for non-normal angles of incidence, and they split into three branches for increasing angles of incidence. All these resonances depend on the grating period p of the nanohole array (Figures S5 and S6).

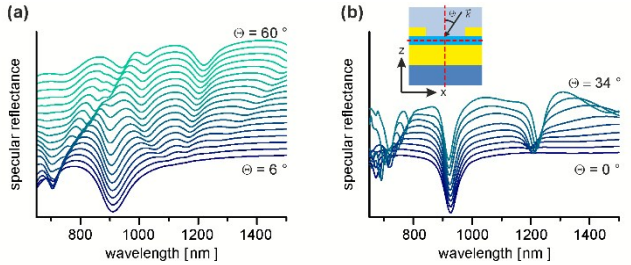

Figure 3. Influence of angle of incidence. Angle-resolved reflectance measurements (a) and FDTD simulations (b) for a sample with p = 570 nm and t_{gap} = 50 nm and p-polarized light. The measurements in (a) were conducted in 3 ° steps. Spectra in (b) were calculated at Θ = 0 °,4 °, 8 °, 14 °, 18 °, 22 °, 26 °, 30 °, 34 °. The angle of incidence is defined in the inset of (b).

Interestingly, the observed optical properties of MIM nanostructures are in stark contrast to that of nanohole arrays without the bottom gold film, which represents a well-characterized system (Figure S4). In order to elucidate the nature of the observed resonances at perforated MIM structures, finite-difference time-domain (FDTD) simulations were employed, and these results were complemented by an analytical theory based on diffraction phase-matching to surface plasmon waves. The modal analysis was performed for non-perforated top gold films, and it revealed that only two surface plasmon modes with transverse magnetic (p) polarization are supported by the MIM structure. The first surface plasmon mode, SP_{air}, propagates at the top Au/air interface. The second gap surface plasmon, SP_{gap}, confines its energy in the PMMA layer sandwiched between two metallic films. This mode exhibits a symmetric profile of the electric field. Moreover, additional anti-symmetric gap surface plasmon can occur but the investigated thicknesses of the PMMA gap t_{gap} < 100 nm are below its cutoff, and therefore this mode is not present.[26]

The light incident at the periodically perforated MIM structure can couple to SP_{air} and SP_{gap} by diffraction. The resonant excitation of these modes occurs when the phase-matching condition is fulfilled, and the real part of the mode propagation constant Re{β} is matched to that of the parallel component of incident light $k_0 \sin(\Theta)$ by the grating momentum $2\pi/p$. In general, the diffraction coupling to surface plasmon modes on a grating with hexagonal symmetry depends on the orientation of the lattice with respect to the incident plane and can occur via different diffraction orders (Figure S7). It is worth noting that the measurements were performed on areas of several mm^2, which is much larger than the single crystalline domain size of the prepared MIM 2D crystal structures. Therefore, the measured resonances due to the diffraction coupling become averaged over different orientations of the lattice.

Figure 3b compares the simulated reflectance spectra with those experimentally measured, which are presented in Figure 3a. Due to the angular dispersion of the plane wave source, the angular range for which the simulation can be carried out is limited. For the smallest angle of incidence Θ = 6 °, two resonances are observed in the measured data at a wavelength of about 690 nm, and 910 nm and simulations predict almost identical results with two resonance dips located at 700 and 900 nm (field distributions are discussed in Figure 4). According to the analytical theory, these two modes are associated with the first and second order diffraction coupling to SP_{gap} and first diffraction order coupling to SP_{air} on a hexagonal grating with p = 570 nm. As can be seen in Figure S7a, the analytical phase matching-based model predicts the appearance of these modes at longer wavelengths of 770 nm and 1200 nm. This discrepancy can be attributed to changes in the propagation constant β due to the perforation, which is not taken into account by the analytical model. When increasing the angle of incidence Θ, the experimentally observed short wavelength resonance splits into two branches, which indicates diffraction coupling. Also, one can see a spectrally broad decrease in the reflectivity in between these two measured branches. However, the simulations indicate a richer spectrum of modes appearing in the same spectral window when increasing the angle of incidence Θ, which can be attributed to the mixing of the second order excitation of SP_{gap} with the first order excitation of SP_{air}. This discrepancy can be attributed to the potential smearing of these features in the measured reflectivity spectrum that can be ascribed to the averaging over differently oriented lattices occurring in the colloidal crystal (see Figure S4a). In contrast to shorter wavelength resonances, the first order SP_{gap} resonance located at about 900 nm does not shift with the angle of incidence Θ as observed experimentally as well as captured by simulations. Instead, a series of dispersive bands appear at longer wavelengths around 1200 nm and 1400 nm when increasing the angle of incidence Θ. The fact that these modes disappear at normal incidence and that the SP_{gap} mode at 900 nm is non-dispersive qualitatively agree with the simulations and can be explained by strong Bragg-scattering of the SP_{gap} modes, which is known to flatten the dispersion relation of propagating surface plasmons.[27]

Following this, we simulated the near-field distribution of electromagnetic field for specific reflectivity dips at normal (Θ = 0 °) and tilted (Θ = 22 °) illumination of the structure with the period of p=570 nm (Figure 4a). The spatial distribution of the electric field intensity $|E|^2$ was normalized with that of the

incident light beam $|E_0|^2$ and showed as a cross-section parallel and perpendicular to the structure (indicated as a dashed line in the inset of Figure 4a). At normal incidence, only two resonances are distinctively visible in the simulated spectra at 923 nm and 670 nm. The corresponding near-field distributions predict an extreme electric field intensity confinement within the gap between the two metal films, indicating a gap-like nature of the resonances (Figure 4c). A dipolar characteristic is clearly apparent for the longer wavelength resonance (B) reaching an enhancement factor $|E|^2/|E_0|^2$ of approximately 25. The resonance at 670 nm (A) shows a higher order field distribution and the field is partially confined outside the structure at the air interface. Thus, these observations agree with the hypothesis of 1st and 2nd order diffraction coupling to SP_{gap} and partial mixing with the excitation of SP_{air} at the outer interface.

Tilting the angle of incidence Θ leads to the splitting of the resonances for different diffraction orders, which are otherwise degenerated and excited simultaneously at normal incidence.[28, 29] Therefore, new resonances are observed in the numerically simulated data between 650 nm and 780 nm and at 1194 nm (Figure 4b). The near-field distribution of the series of resonances noted as I - VI (as indicated in Figure 4b) is presented in Figure 4d. Interestingly, the field distribution of the strongest non-dispersive resonance (V) is not altered by changing the angle of incidence Θ. The electric field maps of the short wavelength modes I – IV show a mixed nature due to the overlap of the $SP_{gap,}$ and the SP_{air} and particularly resonance II exhibits substantial field confinement at the outer interface. When compared with the experiments, probably only mode IV is visible, and the other resonances are smeared by averaging over lattice orientations. The longer wavelength resonances such as VI exhibit solely the SP_{gap} nature as seen in the respective near-field plots. Thus, all resonances, including the non-dispersive modes, can be attributed to either SP_{air} or SP_{gap}. This highlights the simplicity of the given description which provides an alternative view to previous interpretations using magnetic, localized hole plasmons or Fabry-Pérot resonances.[9, 10, 13]

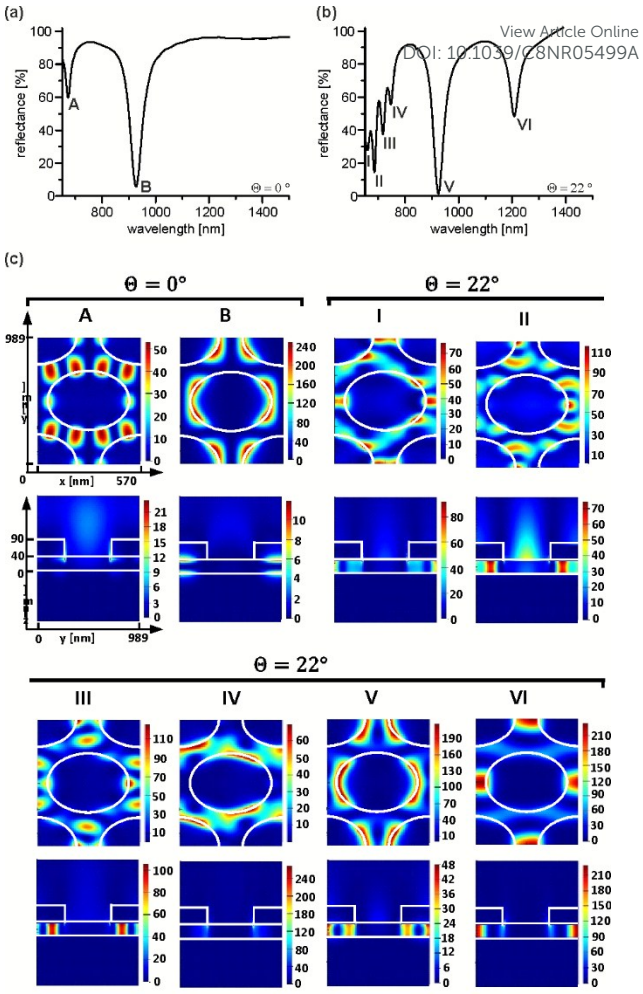

Figure 4. Simulation of the electric near-field distribution. (a) Simulated reflectance spectrum at normal incidence. (b) Simulated reflectance spectrum at Θ = 22 °. (c) Electric field intensity $|E|^2$ distributions normalized to the incident electric field intensity $|E_0|^2$ for the resonance wavelengths assigned in (a) and (b). The electric field enhancement was evaluated along the horizontal and vertical cross-sections shown in the inset of Figure 3b.

The influence of the gap layer thickness was examined experimentally as well as theoretically (Figure 5). In the experiments, the gap PMMA film thickness t_{gap} was controlled between 25 nm and 77 nm by adjusting the spin-coating parameters, and layers with a smaller thickness between 1 nm and 15 nm were prepared using a layer-by-layer approach. When decreasing the thickness t_{gap} from 77 nm to 1 nm, the strongest SP_{gap} resonance drastically shifts from 826 nm to 1417 nm. This observation is confirmed by numerical simulations (see Figure 5b), and the same trend is predicted by the phase-matching model due to the increased propagation constant of SP_{gap} when decreasing the gap thickness t_{gap} (see Figure S7c). Concomitantly, the higher order SP_{gap} resonances become strongly apparent at shorter wavelength, and they shift towards higher wavelengths when decreasing t_{gap}. In contrast, the resonance below 600 nm that is ascribed to the excitation of SP_{air} is weakly affected by changing the gap thickness t_{gap} as only a small portion of its electric field intensity is confined in

the gap. For narrow gaps, gap resonances can be observed even for high angles of incidence (Figure S8 and Figure S9). In contrast, for thick gap layers, all resonances appear in a narrow wavelength range leading to strong coupling between SP_{gap} and SP_{air} modes at larger angles of incidence (Figure S10 and Figure S11). This results in a mixed nature of the resonance at large angles of incidence showing a dispersive behavior.

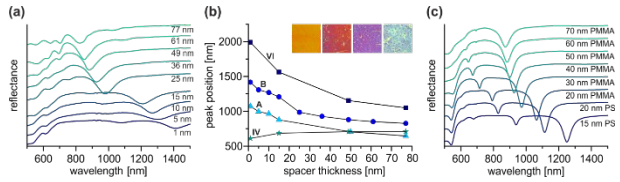

Figure 5. Influence of gap thickness. (a) Reflectance of MIM structures with distinct gap thickness measured at $\Theta = 10°$ with unpolarized light. Gap layers with a thickness of $t_{gap} < 20$ nm were prepared using a layer-by-layer approach. Layer thicknesses with $t_{gap} > 20$ nm were prepared by spin-coating of PMMA. (b) Peak positions in dependence on the gap thickness obtained from reflectance measurements. Modes IV and VI were extracted from angle-resolved measurements. The inset shows macroscopic photographs of 7×7 mm² MIM structures with gap thickness $t_{gap} = 32$ nm, 40 nm, 61 nm, and 77 nm. (c) Simulated reflectance of MIM structures with distinct gap thickness for normal incident light.

A complementary approach to shed light on the observed resonances was performed based on examining the influence of variations of the refractive index environment. For this purpose, the samples were immersed in glycerine-water mixtures with different compositions. Thereby, the refractive index above the structure can be tuned between 1.33 (pure water) and 1.47 (pure glycerine). At first, the effect of the surrounding medium was analyzed using the as-prepared MIM structure (p = 570 and $t_{gap} = 50$ nm). When increasing the surrounding refractive index from 1.33 to 1.47, the SPP confined to the outer Au interface (SP_{air}) shifts to longer wavelengths by approximately 53 nm (Figure 6a). In accordance with the field profiles predicted by numerical simulations, the resonances occurring at longer wavelengths (SP_{gap}) are not sensitive to changes in the refractive index as their electric field is mainly confined inside the structure.

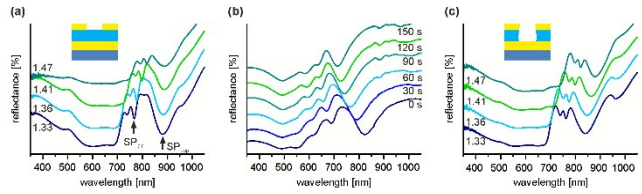

Figure 6. Refractive index sensitivity. (a) Reflectance of the as-prepared MIM structure immersed in glycerine-water mixtures with distinct refractive indices. (b) Reflectance of the MIM structures in air after different times of plasma etching. (c) Reflectance of the MIM structure etched for 150 s, immersed in glycerine-water mixtures with distinct refractive indices.

Next, capitalizing on the organic gap layer, we varied the refractive index of the dielectric gap layer with an initial thickness of $t_{gap} = 51$ nm by plasma etching (Figure 6b). In consecutive etching steps, the PMMA within the holes of the nanohole array is gradually removed until the bottom gold layer is reached after 120 s. This can be inferred from the increasing depth of the holes measured by atomic force microscopy (see Figure S12). Nevertheless, the distance between the metal films and the homogeneity of the sample are not affected. Due to the strongly decreasing refractive index environment in the gap, all resonances (including SP_{gap}) are shifting to shorter wavelengths. Further etching results in an ongoing shift of the resonance wavelength as now the gold-covered PMMA between the holes is removed (underetching). Thus, a quasi-free-standing nanohole array is produced. The smallest shift of 54 nm after 150 s is observed for the mode confined to the Au/air interface (SP_{air}). A higher sensitivity to a change in the refractive index was expected for the gap modes because of the high electric field intensities within the dielectric gap. Indeed, a strong spectral shift from 824 nm to 714 nm is seen for SP_{gap} resonance. We then immersed the MIM sample with a quasi-freestanding nanohole array into glycerine-water mixtures (Figure 6c). Thus, the liquid medium can penetrate the nanohole arrays and change the refractive index between the two gold films. As expected, with a spectral shift of 60 nm, the sensitivity of the SP_{air} resonance in the etched sample is comparable to the non-etched sample. At the same time, the resonance wavelength of the SP_{gap} mode is now strongly influenced. A shift of 39 nm can be observed when increasing the surrounding refractive index from 1.33 to 1.47. Altogether, the sensitivity of the MIM-stack results in 379 nm/RIU and 429 nm/RIU for the SP_{air} mode in the unetched and etched sample and 279 nm/RIU for the SP_{gap} mode.

Conclusions

In summary, we demonstrated the production of trilayer MIM cavities via a simple bottom-up approach. By using an interface-mediated transfer of gold nanohole arrays prepared via nanosphere lithography, high-quality metamaterials were fabricated with square centimeter areas. We thoroughly characterized the optical properties of the resulting MIM stacks composed of an opaque gold film, a polymer gap layer and a second gold film comprising the nanohole array. The rich plasmonic response can be assigned to only two propagating surface plasmon modes, which are strongly dependent on the grating period of the nanohole array and the thickness of the dielectric gap. The symmetric SP_{gap} resonance is insensitive to the angle of incidence and shows an unusually high Q-factor for self-assembled materials comparable to those prepared by top-down lithography techniques. The detailed understanding of the presented phenomena in combination with absorbing layers is of great importance for light harvesting devices.[4, 30, 31]

Materials and methods

View Article Online
DOI: 10.1039/C8NR05499A

Materials: Polystyrene particles were purchased at Microparticles GmbH (Berlin).

Fabrication of ZnO coated substrates: The ZnO layers were prepared using a sol-gel method. For this, glass slides were cleaned for 10 min by ultrasonication in 2 % aqueous Hellmanex (Hellma GmbH, Mühlheim, Germany) solution in MilliQ water. After rinsing off the surfactant with MilliQ water, the substrates were further sonicated for 10 minutes in ethanol and finally dried with compressed air. Subsequently, the ZnO films were formed by spin coating a zinc acetate solution (110 mg zinc acetate in 30 µl 2-aminoethanol and 1 ml 2-methoxyethanol) at 2000 rpm for 50 s and subsequent baking at 150 °C for 5 min.

Fabrication of Au nanomeshes: Monolayers of polystyrene particles were prepared according to the procedure of Retsch *et al.*[21] Cationically functionalized glass slides were spin-coated with a 3 wt% particle dispersion at 4000 rpm. Subsequently, the coated glass substrates were immersed into a 0.1 mM SDS solution in MilliQ. The aqueous phase was adjusted to pH 12 by adding a few drops of NH_3. A monolayer was formed at the liquid/air interface by self-assembly of the detaching particles. The monolayer was transferred to the ZnO coated glass substrates and dried in air. The monolayers were etched in a plasma reactor MiniFlecto (Plasma Technology GmbH, Herrenberg, Germany) with 75 % argon and 25 % oxygen at 80 W at a pressure of 0.14 mbar to obtain non-close packed monolayers. A 3 nm chromium layer and 50 nm gold were deposited using a Balzers BA360 thermal evaporation chamber. The layer thickness was monitored via an SQM 160 microbalance (Sigma Instruments, Schaefer Technologie GmbH). Afterward, the particles were removed using Scotch® tape (3M) giving the nanohole arrays. The Au substrates were cleaned by ultrasonication for 10 min in THF and dried with compressed air. All samples were stored under inert gas.

Fabrication of MIM structures: 100 nm gold was deposited on cleaned microscopy slides. Subsequently, the gap layer was prepared by spin-coating commercially available poly(methyl methacrylate) (PMMA). Thin gap layers (1 nm – 15 nm) were made via a layer-by-layer approach. For this, one layer of polyethyleneimine followed by alternating layers of poly(styrene sulfonate) and poly(allylamine hydrochloride) were applied by spray-coating. The Au nanohole arrays were detached from their parental substrate by immersion into an aqueous hydrochloric acid solution (pH 1) with a speed of 1 mm/min and an immersion angle of 45 ° using a home built dip-coater system. After complete detachment of the gold film, the nanohole array is transferred when lifting the receiving substrate out of the water phase.

Characterization: UV-vis-NIR spectra were measured using the Diffuse Reflectance Accessory of a Cary 5000 UV-vis-NIR Spectrophotometer (Agilent Technologies) at 10 ° angle of incidence with unpolarized light. Angle-resolved UV-vis-NIR spectroscopy was conducted with the Universal Measurement Accessory of the same spectrometer with 3 ° increment with p- and s-polarized light. To examine the effect of the refractive index environment the samples were immersed in glycerine/water mixtures with refractive indices of 1.33 (pure water), 1.36 (20 % glycerine), 1.41 (60 % glycerine) and 1.47 (pure glycerine).

SEM images were taken on a LEO 1530 Gemini Field Emission SEM (Carl Zeiss AG, Oberkochen, Germany). The images were evaluated with the software ImageJ.[32]

Atomic force microscopy was performed in tapping mode on a Dimension 3100 microscope (Veeco, USA) with a Nanoscope IV controller and OTESPA-R3 (Bruker) cantilevers. The AFM images were analyzed with the software Nanoscope Analysis.

FDTD simulations: A commercial package by Lumerical that relies on the finite-difference time-domain method was used to simulate optical properties of gold nanomeshes.[33] As shown in Figure S13, a rectangular unit cell with the hexagonal arrays of holes was used. Bloch boundary conditions were applied at the interfaces of the unit cell that are perpendicular to the structure surface while perfectly matched layers were used on its top and bottom. The investigated structure was approximated by a stack of a perforated gold layer with the thickness of t_{hole} = 50 nm, an intermediate layer of PMMA with a thickness of t_{gap} and a flat fold layer with a thickness of t_{gold}=100 nm. Refractive index of PMMA of n_{PMMA} = 1.4848 was used in the whole spectral range, and the refractive index of gold was determined by fitting to CRC data.[34] The BK7 glass substrate with $n_{substrate}$ = 1.52 was assumed below the plasmonic stack of layers. The excitation light was generated with a plane wave source in the air above the structure, and it was made incident on the perforated gold film. In the used version of FDTD solutions, planar sources exhibit angular dispersion if the beam does not propagate normal to the source. To minimize the angular dispersion, simulations were carried out for wavelength range 550 nm to 900 nm and 900 nm to 1500 nm separately, and the spectra were subsequently stitched. Field intensity and power monitors were placed above or below the unit cell in order to obtain reflectivity and transmission spectra. Electric near-field intensity profiles were calculated by using monitors placed inside the structure.

Acknowledgments

The work in Bayreuth was funded by the German Research Foundation (DFG) by the SFB840. C.S. acknowledges support from the Elite Network of Bavaria (ENB). The authors thank Dr. Beate Förster and Martina Heider from the Bavarian Polymer Institute (BPI) for their support using the scanning electron microscopy facilities. J.D. and S.F. was supported by European Union's Horizon 2020 research and innovation programme under grant agreement no 633937, project ULTRAPLACAD.

Conflicts of interest

There are no conflicts to declare.

References

1. T. W. Ebbesen, H. J. Lezec, H. F. Ghaemi, T. Thio and P. A. Wolff, *Nature*, 1998, **391**, 667-669.

2. N. Sharma, H. Keshmiri, X. Zhou, T. I. Wong, C. Petri, U. Jonas, B. Liedberg and J. Dostalek, *J. Phys. Chem. C*, 2016, **120**, 561-568.
3. D. Inoue, A. Miura, T. Nomura, H. Fujikawa, K. Sato, N. Ikeda, D. Tsuya, Y. Sugimoto and Y. Koide, *Appl. Phys. Lett.*, 2011, **98**, 093113.
4. C. Stelling, C. R. Singh, M. Karg, T. A. F. König, M. Thelakkat and M. Retsch, *Sci. Rep.*, 2017, **7**, 42530.
5. J. Zhu, X. Zhu, R. Hoekstra, L. Li, F. Xiu, M. Xue, B. Zeng and K. L. Wang, *Appl. Phys. Lett.*, 2012, **100**, 143109.
6. A. J. Morfa, E. M. Akinoglu, J. Subbiah, M. Giersig and P. Mulvaney, *J. Appl. Phys.*, 2013, **114**, 054502.
7. C. Hu, Z. Zhao, X. Chen and X. Luo, *Opt. Express*, 2009, **17**, 11039.
8. F. Cheng, X. Yang, D. Rosenmann, L. Stan, D. Czaplewski and J. Gao, *Opt. Express*, 2015, **23**, 25329-25339.
9. P. Pitchappa, C. P. Ho, P. Kropelnicki, N. Singh, D.-L. Kwong and C. Lee, *J. Appl. Phys.*, 2014, **115**, 193109.
10. G. Behera and S. A. Ramakrishna, *J. Phys. D-Appl. Phys.*, 2016, **49**, 075103.
11. T. Maurer, P.-M. Adam and G. Lévêque, *Nanophotonics*, 2015, **4**, 363-382.
12. S. Shu and Y. Y. Li, *Opt. Lett.*, 2015, **40**, 934-937.
13. G. Tagliabue, C. Höller, H. Eghlidi and D. Poulikakos, *Nanoscale*, 2014, **6**, 10274-10280.
14. Z. Fang, Y.-R. Zhen, L. Fan, X. Zhu and P. Nordlander, *Phys. Rev. B: Condens. Matter*, 2012, **85**.
15. M. Mayer, M. Tebbe, C. Kuttner, M. J. Schnepf, T. A. Konig and A. Fery, *Faraday Discuss.*, 2016, **191**, 159-176.
16. N. Vogel, C. K. Weiss and K. Landfester, *Soft Matter*, 2012, **8**, 4044-4061.
17. Z. Wu, X. Chen, M. Wang, J. Dong and Y. Zheng, *ACS Nano*, 2018, **12**, 5030-5041.
18. R. Ortuño, C. García-Meca, F. J. Rodríguez-Fortuño, J. Martí and A. Martínez, *Phys. Rev. B*, 2009, **79**.
19. C. Stelling and M. Retsch, *Adv. Mater. Interfaces*, 2018, **5**, 1800154.
20. C. Stelling and M. Retsch, *Adv. Mater. Interfaces*, 2018, DOI: doi.org/10.1002/admi.201870048.
21. M. Retsch, Z. Zhou, S. Rivera, M. Kappl, X. S. Zhao, U. Jonas and Q. Li, *Macromol. Chem. Phys.*, 2009, **210**, 230-241.
22. N. Vogel, S. Goerres, K. Landfester and C. K. Weiss, *Macromol. Chem. Phys.*, 2011, **212**, 1719-1734.
23. M. Parchine, J. McGrath, M. Bardosova and M. E. Pemble, *Langmuir*, 2016, **32**, 5862-5869.
24. K. Volk, J. P. S. Fitzgerald, P. Ruckdeschel, M. Retsch, T. A. F. König and M. Karg, *Advanced Optical Materials*, 2017, **5**, 1600971.
25. A. Christ, G. Leveque, O. J. Martin, T. Zentgraf, J. Kuhl, C. Bauer, H. Giessen and S. G. Tikhodeev, *J. Microsc.*, 2008, **229**, 344-353.
26. J. A. Dionne, L. A. Sweatlock, H. A. Atwater and A. Polman, *Phys. Rev. B: Condens. Matter*, 2006, **73**, 035407.
27. W. L. Barnes, T. W. Preist, S. C. Kitson and J. R. Sambles, *Phys. Rev. B: Condens. Matter*, 1996, **54**, 6227-6244.
28. H. Ghaemi, T. Thio, D. Grupp, T. Ebbesen and H. Lezec, *Phys. Rev. B: Condens. Matter*, 1998, **58**, 6779-6782.
29. M. Couture, Y. Liang, H. P. Poirier Richard, R. Faid, W. Peng and J. F. Masson, *Nanoscale*, 2013, **5**, 12399-12408.
30. I. Diukman, L. Tzabari, N. Berkovitch, N. Tessler and M. Orenstein, *Opt. Express*, 2011, **19 Suppl 1**, A64-71.
31. C. Fei Guo, T. Sun, F. Cao, Q. Liu and Z. Ren, *Light-Sci. Appl.*, 2014, **3**, e161.
32. W. S. Rasband, ImageJ, U. S. National Institutes of Health, Bethesda, Maryland, USA, http://imagej.nih.gov/ij, 2016).
33. Lumerical Inc., http://www.lumerical.com/tcad-products/fdtd/).
34. J. H. Weaver and H. P. R. Frederikse, in *CRC Handbook of Chemistry and Physics*, ed. D. R. Lide, CRC Press, Boca Raton, 2005, ch. 12, pp. 33-156.

View Article Online
DOI: 10.1039/C8NR05499A

Metal-insulator-metal structures prepared by self-assembly exhibit narrow gap plasmon modes, which are fully described by analytical theory.

View Article Online
DOI: 10.1039/C8NR05499A

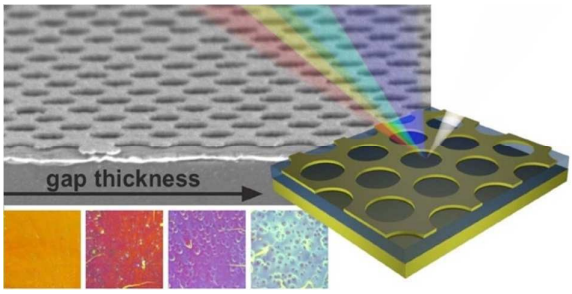

Metal-insulator-metal structures prepared by self-assembly exhibit narrow gap plasmon modes, which are fully described by analytical theory.